



Anastasios Tsikouras

**Heat transfer validation of the thermal interface of the new
Compact Bolometer Camera in the W7-X reactor**

IPP 2024-13
April 2024

Heat transfer validation of the thermal interface of the new Compact Bolometer Camera in the W7-X reactor

Internship report

Anastasios Tsikouras

Supervisors:
Josefine Proll
Felix Reimold

Eindhoven, February 2023

Abstract

In the Wendelstein 7-X stellarator reactor, the radiated power of the plasma is a parameter providing useful information about the performance of the machine. Bolometer cameras are employed to measure this parameter and its data can contribute to control purposes. As space for diagnostics is limited, a new camera was designed for providing data from multiple cross-sections, by allowing installation in already occupied diagnostic ports. The conductivity of the interface material between the camera and the reactor's cooling pipes must be validated, to assure the safety of both the camera and the reactor, since the camera will be passively cooled. With a small-scale experiment using mock-ups of the camera base and the cooling pipes, several case studies were investigated. The results provide validation of the interface material conductivity and the geometric parameters of the interface were optimized for the most efficient heat transfer

Preface

Contents

Contents	vii
List of Figures	ix
List of Tables	xi
1 Introduction	1
2 Background	5
2.1 Theory	5
2.2 Thermoelectric heat pumping	6
3 The experiment	9
3.1 Experimental Description	9
3.2 The Experimental equipment	9
3.2.1 Temperature control	9
3.2.2 The mock-up	10
3.2.3 The vacuum chamber	11
3.3 The Experiment	11
3.3.1 Procedure in vacuum	11
3.3.2 Procedure in air	12
3.4 1D heat transfer model	13
3.4.1 Thermal resistance modelling	13
3.4.2 1D thermal model validation	14
3.5 Cases studied	16
4 Data post-processing	17
4.1 Clearing the data	17
4.2 Identifying the applied power	18
4.3 Effective conductivity	20
4.4 Thermal contact conductance	20
4.5 Data uncertainty	21
4.5.1 Materials	21
4.5.2 Measurements	21
5 Results	23
5.1 Conductivity estimate.	23
5.2 Thermal contact conductance estimate.	26
5.3 Validation of the results.	28
5.4 Curved and negative mock-ups	29
5.5 Steel-sigraflex extrapolation analysis	31
5.6 Simulations on the full CBC model	32

6 Conclusions	35
Bibliography	37
Appendix	39
A Appendix	39

List of Figures

1.1	CAD model of the 6-channel Compact Bolometer Camera (CBC). Left: CAD model of the CBC, right: CAD model of the CBC mounted on the portliner.	2
1.2	Line-of-sight of CBC schematic for two regions. Left: wide spread of the lines of sight, right: narrow spread of the lines of sight focusing on the divertor.	2
2.1	Peltier element power balance.	6
2.2	Peltier element power balance simplified.	7
3.1	The Arduino setup for the purpose of temperature control and temperature reading.	10
3.2	The tested mock-ups (negative flat and curved profiles). Left: individual parts, right: assembled along with the sigraflex foil as an interface	10
3.3	Left: the vacuum chamber of the lab, right: all individual parts of the setup	11
3.4	The experimental setup assembled. Left: the mock-up with the sensors' positions and the aluminum block, right: top view of the setup.	12
3.5	Sketch of the ridges simplified geometry.	13
3.6	Simulation setup in the SimScale environment for the flat mock-up. Simulation parameters: $l_{sigraflex} = 0.8mm$, $k_{sigraflex} = 2.38W/mK$, $Q_{applied} = 50W$, $T_{hot} = 100^{\circ}C$	15
3.7	Comparison of simulations with the 1D constructed model for two different applied powers. Top left: Simulation for $Q_{applied} = 50W$, top right: model results for $Q_{applied} = 50W$, bottom left: Simulation for $Q_{applied} = 100W$, bottom right: model results for $Q_{applied} = 100W$. Material parameters used: $l_{sigraflex} = 0.8mm$, $k_{sigraflex} = 2.38W/mK$, $k_{aluminum} = 130W/mK$	15
4.1	Typical experimental measurement graph. Top figure: temperature evolution on the different components used in the experiment. blue: temperature on the top of the mock-up, orange: temperature on the bottom of the mock-up, red: first temperature on the aluminum block, purple: second temperature on the aluminum block. Bottom figure: temperature difference on the mock-up edges with respect to time. The vertical red lines indicate the constant temperature difference part used for the analysis.	17
4.2	Temperature evolution on the aluminum block set on the top of the mock-up for the identification of the power absorbed from the Peltier element.	19
4.3	Calculated convection coefficient for the lab environment air. The red dashed lines indicate the valid part of the estimation	20
5.1	Estimated thermal conductivity of sigraflex, for the assumption of perfect thermal contact with aluminum. The grey area represents the uncertainty of the calculation.	23
5.2	Thermal conductivity of sigraflex comparison, for the assumption of perfect thermal contact with aluminum, for the case study of different applied powers.	24
5.3	Thermal conductivity of sigraflex comparison, for the assumption of perfect thermal contact with aluminum, for the case study of different applied torques.	25

5.4	Thermal conductivity of sigraflex comparison, for the assumption of perfect thermal contact with aluminum, for the case study of different numbers of foils.	25
5.5	Break-up of the individual parts of the interface thermal resistance. Top: first contact part, middle: sigraflex bulk part (The term "TIM" refers to "Thermal Interface Material"), bottom: second reduced area part.	26
5.6	Comparison of thermal contact conductances for the different number of foils along with the aluminum-aluminum case.	27
5.7	Comparison of thermal contact resistances for the different interface materials. . .	27
5.8	Comparison of the simulated temperature difference across the flat mock-up (blue) with the experimental temperature difference (orange).	28
5.9	Comparison of simulation and experimental data for the achieved ΔT for the curved mock-up.	29
5.10	Comparison of the temperature difference between the flat and negative CBC base mock-up.	30
5.11	Temperature difference across the mock-up for steel properties. The results were produced from the 1D model, for steel conductivity: $k_{steel} = 45 \text{ W/mK}$ and for the sigraflex parameters of each experiment. The applied power flux: 120 kW/m^2 . . .	31
5.12	Investigation of the conductance variation of the steel-sigraflex contact on the heat transfer, for the reactor-relevant heat load of 120 kW/m^2 . The reference of this analysis is the best case of the aluminum case study (marked in blue) taken from Figure 5.11. The investigated conductance values are random due to the lack of evidence for the thermal contact conductance of steel with sigraflex.	32
5.13	Simulation on the full CBC model. Top: outer view of the CBC model, Bottom: inside view of the CBC model. The channel base plate is indicated with the arrow	33
A.1	Calculated conductances for the two case studies. Right: different applied power, left different applied torque.	39
A.2	Simulated temperatures on the top mock-up plate. Temperatures were taken in the middle of the plate, sensor position, edge of the plate and average temperature of the plate. Left: simulation for the low found conductivity, right: simulation for the high found conductivity.	40
A.3	Simulated temperatures on the bottom mock-up plate. Temperatures were taken in the middle of the plate, sensor position, edge of the plate and average temperature of the plate. Left: simulation for the low found conductivity, right: simulation for the high found conductivity.	40

List of Tables

3.1	Description of the parameters used for the validation of the 1D model with the SimScale simulation.	14
3.2	Deviation of the model's temperature difference across the mock-up surfaces from the simulations.	16
3.3	Description of the experiments performed. The percentage represents the duty cycle set in each session while the second number is the applied torque on the mock-up.	16
4.1	Convection coefficient comparison of literature and experimentally calculated values	19
5.1	Experimental parameters for the negative CBC base mock-up.	30

Chapter 1

Introduction

Tokamaks and stellarators are the two most promising experimental fusion reactor designs. Both reactors are devices that magnetically confine plasmas for the ultimate purpose of energy production. Tokamaks create their magnetic configuration by coils and a running current through the plasma, which causes instabilities to occur. Stellarators create their magnetic field exclusively with coils and do not require a plasma current. However, to achieve the desired conditions for fusion, their magnetic configuration is far more complex than the tokamak reactor.

Measuring the radiated power of the plasma can provide information about the power output of the reactor. A profile of the power output can provide information about radiation losses due to impurities and additionally can be used for control of the radiated power in detachment regions, mitigating the power that plasma-facing components receive [1]. In the W7-X stellarator [2], currently the largest stellarator in the world, bolometer cameras are responsible for measuring the power radiated by the plasma. Their working principle is the following: bolometer channels absorb the power radiated along their line-of-sight, acquiring a line-integrated signal. By combining more than one camera that views the same cross-section from different positions, it is possible to perform tomography of the radiated power via calculations on the intersecting lines of sight, acquiring a 2D profile for the respective cross-section. Depending on its viewing geometry, each camera can acquire data from a wide or narrow section of the plasma, as well as focus on targeted areas of interest such as the core or the divertor region. Bolometers have a wide wavelength absorption region, usually from infrared to soft X-rays, and hence their data can determine the total absorbed radiated power in this spectrum. For any bolometry regions, the cameras view only one cross-section of the reactor.

Experimental results show asymmetry of the radiated power caused by asymmetries in the transport of particles/impurities [1]. To observe those asymmetries it is essential to have access to data from different cross-sections and in different folds of the reactor. However, W7-X has limited space for diagnostics. The Transport and Radiation Team of Max Planck Institute of Plasma Physics, has designed a new Compact Bolometer Camera (CBC) which can be more easily adapted to multiple ports and viewing geometries and can fit along with other diagnostics without interfering with them. The new design achieves those goals by being compact, versatile and by forgoing external active cooling, as the camera will be passively cooled by being installed directly on the system of cooling pipes that thermoregulate the inner side of each diagnostic port (portliner), which is connected to the cryostat of the reactor, allowing for cooling via conduction. Figure 1.1 shows the CBC in its CAD form installed in a portliner of W7-X and Figure 1.2 shows two of the potential ports that the CBC is considered to be mounted.

Since the CBC will be mounted inside the reactor without active cooling, it is essential to guarantee both the safety of the reactor and the integrity of the experimental campaign. A malfunction of the equipment may cause severe damage to the reactor or halt the experimental campaign for weeks or months. The new design already underwent preliminary simulations obtaining the first data to conclude whether the camera can withstand the heat loads of the plasma, but the results require verification with experimental data. Especially the thermal resistance of

the contact between the portliner and the bolometer base needs to be assessed experimentally before proceeding with the installation, which is foreseen for the next experimental campaign.

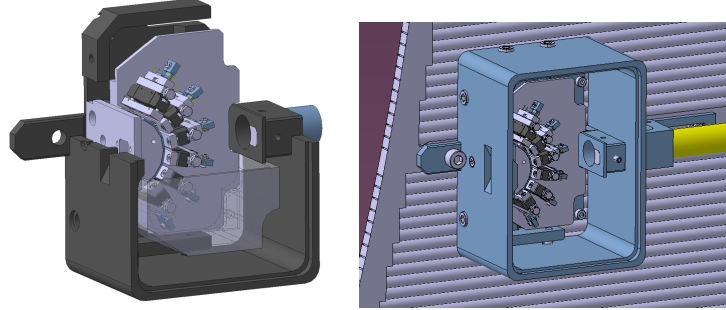


Figure 1.1: CAD model of the 6-channel Compact Bolometer Camera (CBC). Left: CAD model of the CBC, right: CAD model of the CBC mounted on the portliner.

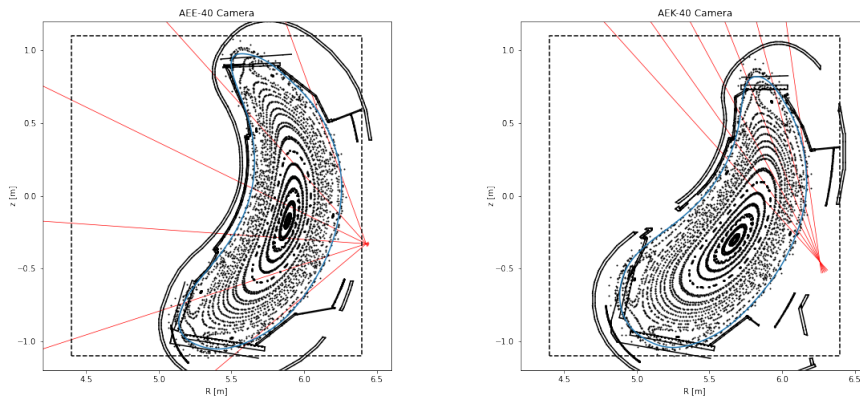


Figure 1.2: Line-of-sight of CBC schematic for two regions. Left: wide spread of the lines of sight, right: narrow spread of the lines of sight focusing on the divertor.

The aim of this paper is the heat transfer validation of the CBC base-portliner interface to ensure the safe operation of the reactor and the faultless operation of the bolometer camera itself. To achieve this goal, the main parameters that need to be validated are the thermal conductivity of the interface layer and the thermal contact conductance of the interface material with the contact areas of the CBC. A mock-up of the portliner profile along with the respective bolometer base was manufactured, with the goal of identifying the thermal conductivity of the interface material between the portliner and camera base.

Besides the heat transfer validation, an analysis is performed by studying how different parameters, namely the number of interface layers and applied torque in the interface material, affect the thermal conductivity in search of the optimal heat transfer setup. Additionally, the same analysis is performed on a second geometry for the CBC base, to investigate the effect of the contact area on the heat transfer, which is expected to be of vital importance. The overall analysis shows promising results which confirm that the CBC can be safely installed in the portliners of W7-X without active cooling for short to medium timewise discharges.

For a quick overview, the report is organized as follows:

- Background: discussion on the theory, formulas and equations used in the analysis.
- The experiment: description of the experimental setup, the procedure followed to perform the experiment, the modelling of the quantities needed for the analysis and the cases that this report studies.
- Data post-processing: discussion of the procedure of identifying the quantities under investigation from the obtained measurements, as well as the role of uncertainty in the final results.
- Results: presentation of the calculated quantities.
- Conclusions: summary of the results and discussion of the outcome.

Chapter 2

Background

2.1 Theory

This chapter is based on the book "A Heat Transfer Textbook", [3]. The main equation used for the identification of the thermal conductivity of a material and the thermal contact conductance of two materials in contact, is Fourier's law of conduction [2.1], which states that for a given applied power in a medium, the temperature gradient is proportional to the conductivity of the material.

$$q = k \cdot \nabla T \quad (2.1)$$

with Q the thermal power applied [W], k the thermal conductivity of the material [W/mK], T the temperature [$^{\circ}$ C].

Additionally, equation 2.2 states that the temperature difference of an object is dependent on the energy applied to the object, on the mass and on the specific heat of the object (uniformity assumed).

$$W = m \cdot c_p \cdot \Delta T \Rightarrow Q = m \cdot c_p \cdot \frac{dT}{dt} \quad (2.2)$$

with W the thermal energy applied [J], m the mass of the object [kg] and c_p the specific heat of the material [W/kg $^{\circ}$ C].

For a material with known mass and thermal properties, by tracing the temperature rise/-decrease with respect to time, the derivative can be calculated. Using equation 2.2, the applied power on the object can be identified.

By solving Fourier's equation for heat transfer in one direction, for a wall of a material with thermal conductivity k , thickness l and area A , equation 2.3 is obtained.

$$Q = \frac{k \cdot A \cdot \Delta T}{l} \quad (2.3)$$

The term $\frac{l}{k \cdot A}$ is the thermal resistance of the wall with units of measurement [K/W].

$$R = \frac{l}{k \cdot A} \quad (2.4)$$

In the case of a two-material wall with thermal conductivities k_1 and k_2 , thicknesses l_1 and l_2 respectively and with the materials being thermally connected serially, Fourier's equation becomes equation 2.5

$$Q = \frac{\Delta T}{\frac{l_1}{k_1 \cdot A} + \frac{l_2}{k_2 \cdot A}} \quad (2.5)$$

with h_c the thermal contact conductance of the two materials or simply conductance [W/m^2K]. The conductance dictates the imperfect touch of the two material surfaces, resulting in a discontinuity in the temperature on the contact surface. If perfect contact is assumed, then $\frac{1}{h_c} = 0$. The reciprocal of the thermal contact conductance, thermal contact resistance, is the inverse of h_c as seen in equation 2.6.

$$R_{h_c} = \frac{1}{h_c} \quad (2.6)$$

The conductance is not a material property, but a quantity that depends on the interface of the two materials, the pressure applied, the surface roughness and more [4]. Equation 2.7 describes the thermal resistance of an interface material that is being "sandwiched" between two others.

$$R = \frac{1}{h_{c,1} \cdot A} + \frac{l}{k \cdot A} + \frac{1}{h_{c,2} \cdot A} \quad (2.7)$$

with $h_{c,1}$ and $h_{c,2}$ the conductances of the interface material with the two contacts on its two sides.

Lastly, power lost to the environment in the form of convection is described in equation 2.8

$$Q = h_{conv} \cdot A_{exposed} \cdot (T - T_{amb}) \quad (2.8)$$

where h_{conv} the convection coefficient [W/m^2K], $A_{exposed}$ the exposed area to the convection medium [m^2], T the temperature of the object and T_{amb} the ambient temperature.

The equations above will help to construct a basic heat transfer model and calculate the conductivity and conductance of the interface material.

2.2 Thermoelectric heat pumping

Peltier modules are thermoelectric elements that take advantage of the Peltier effect. In a simple manner, the Peltier effect states that when current passes through a thermoelectric junction, heat is transferred from one side of the module to the other, causing the temperature to drop on the absorbing side, and the temperature to rise on the depositing side [5].

The heat absorbed at the "cold" side of the element is given by equation 2.9

$$Q_{absorbed} = \alpha \cdot I \cdot T_c \quad (2.9)$$

where α is the seebeck coefficient [V/K], I the current flowing through the element [A], and T_c the temperature at the cold side of the peltier [5].

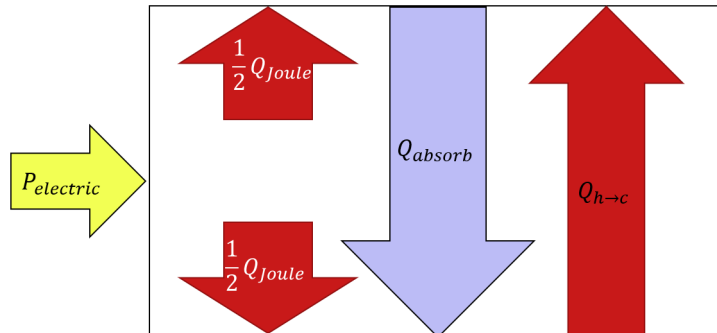


Figure 2.1: Peltier element power balance.

The real power absorbed and deposited in the Peltier module's sides is determined from the thermoelectric heat pumping (equation 2.9) and 2 extra effects: Joule heating (Q_{joule}) and conduction ($Q_{h \rightarrow c}$) from hot to cold side (heat backflow) [5]. Those effects depend on the internal resistance of the Peltier element, as well as on the conduction coefficient of the materials used. Figure 2.1 presents the total heat transfer inside the Peltier element. Overall the power balance on the Peltier element can be summarized as seen in figure Figure 2.2 and in equation 2.10 [6].

The Peltier elements will be part of the experiment and having an insight into their power balance will help in accurately calculating the power delivered on the experimental setup.

$$Q_{hot} - Q_{cold} = P_{electirc} \quad (2.10)$$

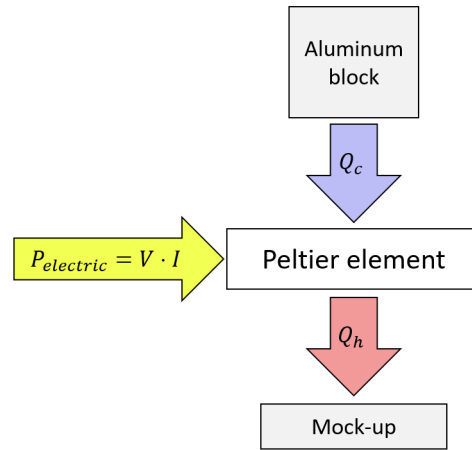


Figure 2.2: Peltier element power balance simplified.

Chapter 3

The experiment

3.1 Experimental Description

The main goal of the experiment is to identify the conductivity of the interface material that will be used as contact between the base of the CBC and the portliner. The experiment consists of an Arduino for temperature control and data acquisition, three aluminum mock-ups for the testing (flat, curved and negative of the portliner), the interface material under investigation and a vacuum chamber as the testing place.

Thermal sensors acquire the temperature data of specific points. For a known applied heat flux and by using Fourier's law of conduction along with the modeled thermal resistances of the different parts, the conductivity of any interface material can be calculated.

Although steel is the material of choice for the real camera, aluminum is used for the experiment to take advantage of its high conductivity and hence the small temperature gradient across its surface. That way, the evaluation of the resistance of the interface material, becomes less complex. For the results of the experiment, the material choice is trivial. If the thermal resistances are modeled correctly, then by a simple change of the material properties in the used equations, the results remain accurate.

3.2 The Experimental equipment

3.2.1 Temperature control

A temperature control system is essential to the experiment, for the precise manipulation of the temperatures across the mock-up. The constructed full setup for temperature control is depicted in Figure 3.1. It consists of one Arduino Megaboard 2560, 8 platinum temperature sensors PT1000, 8 Resistance-to-Digital converters where the sensors are connected and 2 Pololu G2 high-power motor drivers.

The dual purpose of the Arduino is the temperature read on the mock-up and the temperature control/deliver-of-the-heat-flux via PWM through the motor drivers on the mock-up by two Peltier modules.

PWM is a simple way of controlling the power applied to the Peltier elements, by keeping on the applied voltage for a set amount of time in a period. The fraction of the time when the voltage is applied over the period of the pulse is called duty cycle.

Using the Arduino IDE, a program was structured to control the temperature using PWM by modulating the pulse with a PID controller, where the suitable PID coefficients are reset and optimized for each application. The chosen Arduino pins for the PWM allow for 8-bit control, meaning the PWM can be incremented in multiples of $1/255$, or $1/255 \cdot 100\%$ of the full pulse length, which is sufficient for the purposes of this experiment.

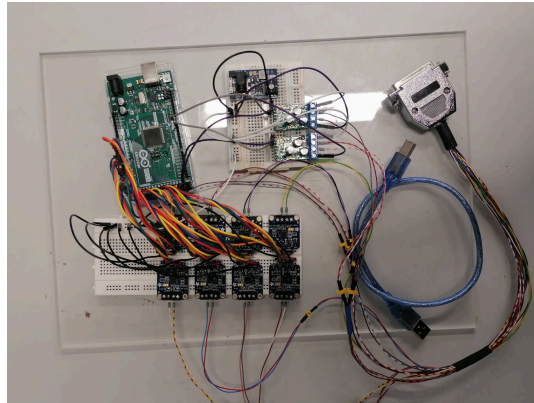


Figure 3.1: The Arduino setup for the purpose of temperature control and temperature reading.

The power absorbed in the cold side of the Peltier element for a specific temperature difference across the Peltier element faces and voltage applied, can be identified using the manual's graph.

3.2.2 The mock-up

The diagnostic ports can have either a flat (rectangular) or a round (circular) profile and so 2 mock-ups are tested: one with surfaces parallel to each other for the flat case, and one with the touching surfaces curved, representing the circular part of the portliner.

All tested mock-ups, in pieces and assembled, are presented in Figure 3.2. The mock-up of the contact surface of the CBC with the portliner of W7-X consists of two aluminum parts, representing the base of the bolometer detectors housing and the cooling pipes of the portliner respectively.

As a supplementary case, the negative profile of the portliner on the CBC base, the top left part of Figure 3.2, was tested to investigate which geometry is more efficient in transferring the heat from the CBC base to the cooling system, for the manufacturing of the CBC base.

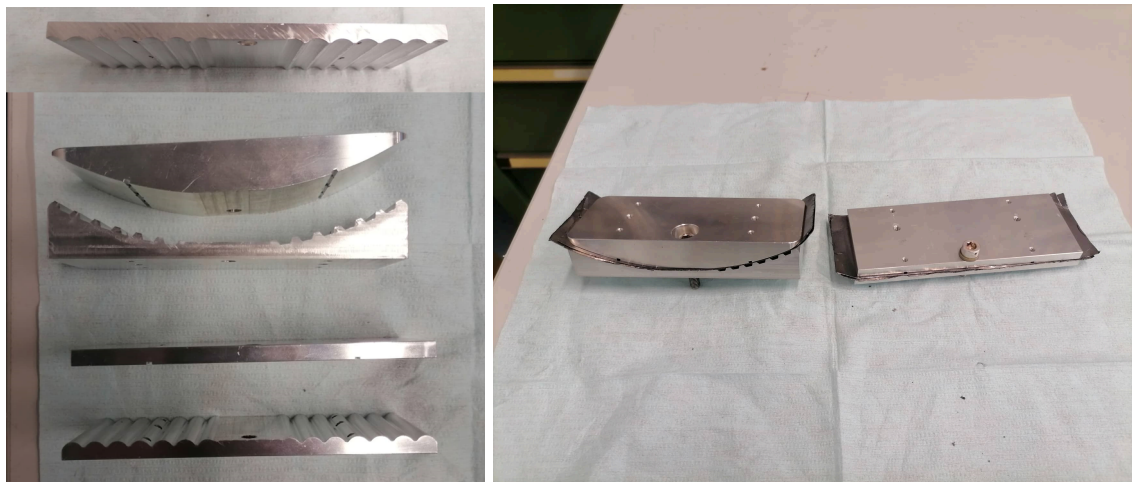


Figure 3.2: The tested mock-ups (negative flat and curved profiles). Left: individual parts, right: assembled along with the sigraflex foil as an interface

The material tested as the interface is sigraflex foil, a thermally anisotropic, flexible graphite foil with high thermal conductivity parallel-to-the-surface direction and poor conductivity on the

direction normal to its surface [7]. Despite the poor conductivity in the direction of interest, the graphite foil is expected to enhance the heat transfer from the camera to the portliner compared to the simple metal-to-metal contact, for two reasons. The conductance of steel with steel is low and the touching surface due to the circular profile of the portliner pipes reduces the contact area of the materials. With a graphite foil interlayer, the contact area is expected to increase as an outcome of its flexibility and compressibility. Additionally, graphite foil is one of the few vacuum-compatible materials compressible and inexpensive.

3.2.3 The vacuum chamber

The vacuum chamber is the preferred place for the experiment to minimize the losses through convection and to simulate the real conditions of the reactor in which the camera will operate.

Besides the chamber, an important component is a flange attached to the side, which allows for electrical connections and water flow inside the chamber. The vacuum chamber along with all the individual parts of the setup are presented in Figure 3.3

Unfortunately due to a dimension mismatch, the ordered flange did not fit in the vacuum chamber port, preventing the use of water cooling for the Peltier elements inside the chamber. Although a few attempts to perform the experiment in vacuum were performed, we observed that the Peltier element responsible for the temperature control of the colder side of the mock-up was heating fast and the temperature on that side could not be controlled. For this reason, the experiment was alternated so that it could be performed without cooling. An elaborate description is discussed in the next section.

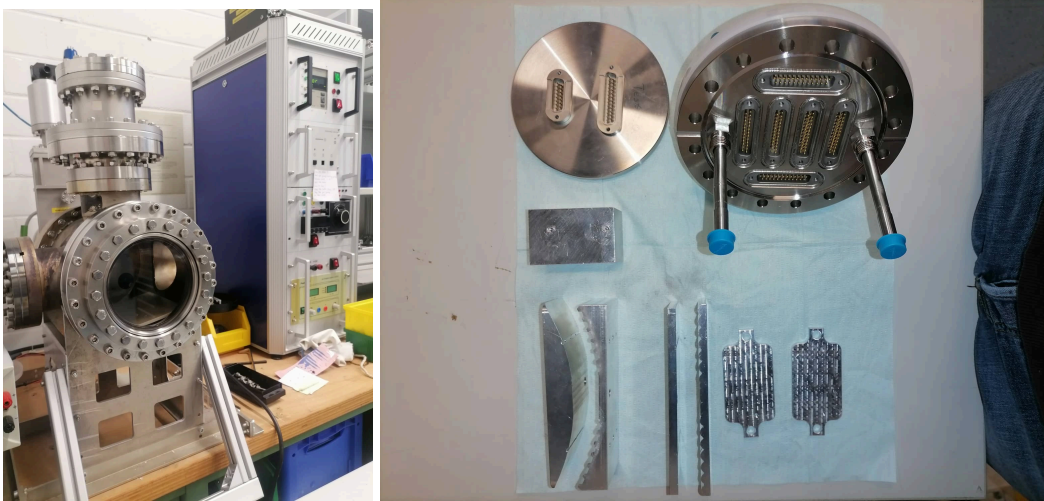


Figure 3.3: Left: the vacuum chamber of the lab, right: all individual parts of the setup

3.3 The Experiment

3.3.1 Procedure in vacuum

As mentioned before, the experiment did not take place in the vacuum chamber. However for completeness purposes, in this section we discuss the proposed procedure.

In vacuum, the material choices are limited due to outgassing. Porous materials, or materials containing elements that evaporate, will outgas [8], resulting in a low-performance vacuum. The assembly consists of aluminum and sigraflex for the mock-up, steel and peek for the bolts. Peek is a thermal insulating polymer material placed between the bolt and the bolt contact with the aluminum to minimize the heat transfer between the mock-up pieces via the bolt. The sensors

were fastened on the mock-up encased in copper casings. To ensure the contact of the sensor with the object, a thin kapton cable presses against the sensor while the copper casing is fastened in various places. Kapton is another vacuum-compatible material that is used for wrapping the cables and, in this case, to ensure the contact of the sensors.

With access to water cooling, the mock-up would be placed inside the vacuum chamber with a copper mesh thermally connecting the sides of the Peltier elements with the water-cooling pipe. After ensuring that the sensors and the Peltier elements work properly, the depressurization of the chamber starts until the pressure drops to $\approx 10^{-7} \text{bar}$, with the combination of a rotary pump and a turbo pump.

When the desired vacuum is reached, using the PID-controlled temperature system, the temperatures at the edges of the mock-up are set and maintained constant for the data acquisition. The useful data are the temperature measurements on the two sides of the mockup, along with the measurements on the opposite sides of the Peltier elements. The latter measurements will determine the cooling power of the Peltier elements, using the Peltier datasheet. At thermal equilibrium, the temperature difference should be constant and the post-processing of the data is possible.

Without water cooling, the experiment implementation was difficult in vacuum for two reasons. After the heating of the mock-up, there are no means for the thermal energy to be dissipated, except radiation, which made the repeatability of the experiment time-consuming. Most importantly, the Peltier element responsible for cooling the mock-up was heating up rapidly, losing its ability to maintain a constant temperature, with the potential danger of damaging the Peltier module.

3.3.2 Procedure in air

Without water cooling available neither inside nor outside the vacuum chamber, the procedure was modified for the experiment to be successful. The change in the environment does not affect the final results, because the conductivity is not a property affected by environmental conditions, as long as there is an accurate estimation of the power delivered in the mock-up. The power estimation becomes more complicated in this case, due to the convection power exchange between the experimental setup and the environment. This effect will be discussed in the next chapter.

Instead of two Peltier elements for temperature control on both sides, one Peltier element is used at a constant PWM duty cycle, delivering approximately constant power flux on the mock-up [9]. Using this method, the measured temperatures on the sides of the mock-up are not constant. However, the temperature difference across the two sides, following Fourier's law, should be constant. The assembled setup of the experiment is presented in Figure 3.4.

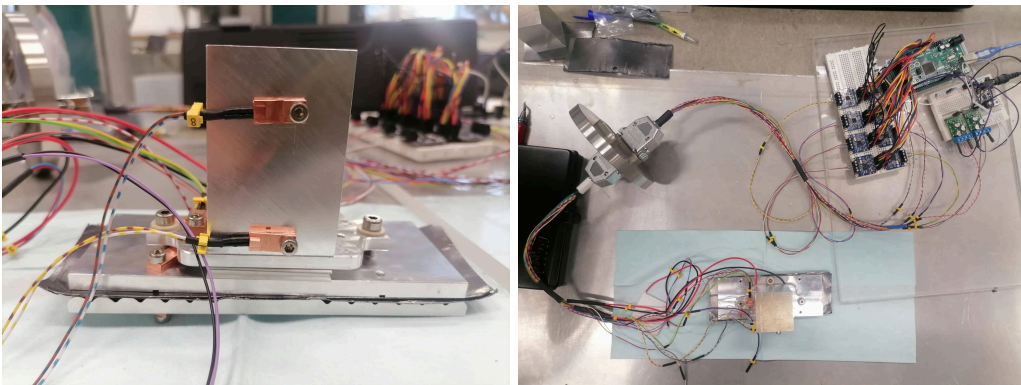


Figure 3.4: The experimental setup assembled. Left: the mock-up with the sensors' positions and the aluminum block, right: top view of the setup.

Differently from the vacuum procedure, a solid block of aluminum is placed on top of the outer side of the Peltier module which serves the purpose of identifying the power dissipated in the

mock-up, by studying the temperature change on the block. As the temperatures on both sides of the Peltier element are not constant, the datasheet table is not useful anymore.

3.4 1D heat transfer model

3.4.1 Thermal resistance modelling

For the calculations in the analysis, it is important to have an understanding and a proper model of the thermal resistance of each part of the mock-up. The accuracy of the thermal resistances can be checked with a basic 1D heat transfer model of the mock-up which assumes heat transfer only in the normal to the surface direction. Each thermal resistance is calculated by solving Fourier's equation of heat transfer, with suitable parameters. For all the parts with constant area along the cross-sections, the thermal resistance of each part is equal to equation 2.4 from section 2, with k and l the conductivities and thicknesses of each material.

The ridged aluminum part is treated as a combination of a piece including only the ridged part, and a solid block with the rest of the mass. For the ridged part, the area is a function of the distance from the edge, and hence this needs to be included in Fourier's equation before attempting to solve it. For simplicity, it is assumed that the ridges are canonical trapezoids with $a/b = f$, where f is the reduction factor of the touching area over the area at the end of the ridges. Figure 3.5 visualizes all the geometric considerations of the simplified ridged part of the mock-up.

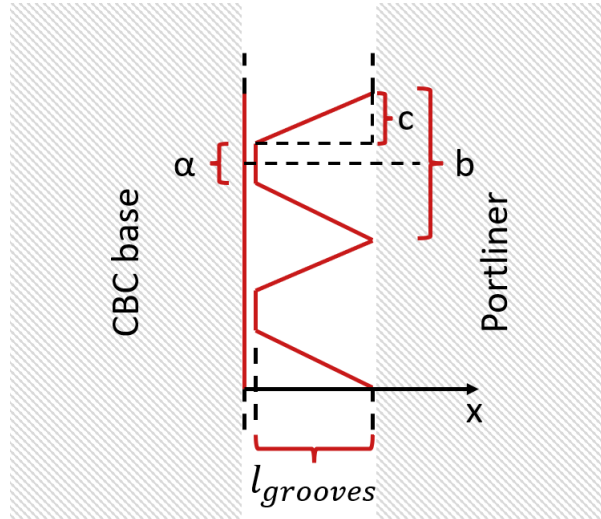


Figure 3.5: Sketch of the ridges simplified geometry.

The area with respect to the distance x from the edge of the mock-up follows equation 3.1

$$A_{grooves} = (a + c) \cdot N \cdot t \quad (3.1)$$

where, a is the initial thickness of the trapezoid, c the base of the triangle as seen in Figure 3.5 and t the thickness of the part.

Using the relations 3.2, 3.3 and 3.4, we derive equation 3.5, which represents the area change of this part of the mock-up with respect to the distance x from its edge.

$$\frac{a}{b} = f \quad (3.2)$$

$$\frac{c}{x - (l_1 + l_2)} = \frac{b}{l_{rig}} \quad (3.3)$$

$$A_{tot} = b \cdot N \cdot t \quad (3.4)$$

$$\begin{aligned} A_{rigids} &= (a + c) \cdot N \cdot t = \left[f \cdot b + \frac{[x - (l_1 + l_2)] \cdot b}{l_{rig}} \right] \cdot N \cdot t = \\ &= \left[f + \frac{x - (l_1 + l_2)}{l_{rig}} \right] \cdot b \cdot N \cdot t = \\ &= \left[f + \frac{x - (l_1 + l_2)}{l_{rig}} \right] \cdot A_{tot} \end{aligned} \quad (3.5)$$

By inputting the area in Fourier's equation the following derivation for the ridged part of the piece is obtained.

$$\begin{aligned} Q &= A \cdot k \cdot \frac{dT}{dx} = \\ &= \left[f + \frac{x - (l_1 + l_2)}{l_{rig}} \right] \cdot A_{tot} \cdot k \cdot \frac{dT}{dx} \Rightarrow \\ \Rightarrow Q &= \frac{k \cdot A \cdot \Delta T}{l_{ridged}} \cdot \frac{(1 - f)}{\ln \frac{f + (x - l_{al,1} - l_{sigraflex}) \cdot (1 - f) / l_{ridged}}{f}} \end{aligned} \quad (3.6)$$

The summary of all the thermal resistances for every part of the mock-up is given below. For the ridged component, the resistance is found for $x = l_{ridged} + l_{al,1} + l_{sigraflex}$. The 1-D model created is based on those equations, and for a given heat load and boundary condition temperature, the temperature profile inside the mock-up is estimated.

$$R_{al,1} = \frac{l_{al,1}}{k_{al} \cdot A_{plate}} \quad (3.7)$$

$$R_{sigraflex} = \frac{l_{sigraflex}}{k_{sigraflex} \cdot A_{plate}} \quad (3.8)$$

$$R_{al,ridged} = \frac{l_{ridged}}{k_{al} \cdot A_{plate}} \cdot \frac{\ln 1/f}{1 - f} \quad (3.9)$$

$$R_{al,compact} = \frac{l_{al,compact}}{k_{al} \cdot A_{plate}} \quad (3.10)$$

3.4.2 1D thermal model validation

Since this 1D modeling of the thermal resistances will be used to perform the calculations of the conductivity and conductance of the mock-up, it is important to verify that the model is accurate. This is achieved by comparing the temperature difference across the mock-up sides of the model with the temperature gradients predicted for the same applied power by a SimScale simulation [10] of the heat transfer. For an accurate comparison, the same parameters are used for different applied powers. Specifically, Table 3.1 shows the parameters used for both the model and the simulation setup.

Material parameters/boundary conditions			
k [W/mK]	foil thickness [mm]	T_{hot} °C	$Q_{applied}$ [W]
2.38	0.8	100	50-100

Table 3.1: Description of the parameters used for the validation of the 1D model with the SimScale simulation.

To accurately compare the simulation with the model, since the model assumes that the boundary conditions are applied to the whole surface of the mock-up, in the simulations the boundary conditions are also applied to the whole surface. It is visible from Figure 3.6 that a temperature gradient is present in the bottom plate of the mock-up of the simulation due to the power flux boundary condition. Hence for the comparison, the mean temperature of the surface will be taken into account.

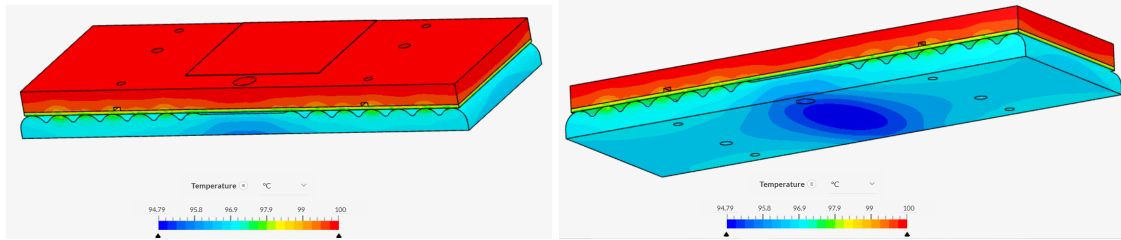


Figure 3.6: Simulation setup in the SimScale environment for the flat mock-up. Simulation parameters: $l_{sigraflex} = 0.8mm$, $k_{sigraflex} = 2.38W/mK$, $Q_{applied} = 50W$, $T_{hot} = 100^{\circ}C$

The comparison was made for two different heat loads, as presented in Figure 3.7, to investigate how the error propagates for different powers. Indeed it can be seen that there is a match between the temperature differences of the simulation and the model with a variation of less than 2%.

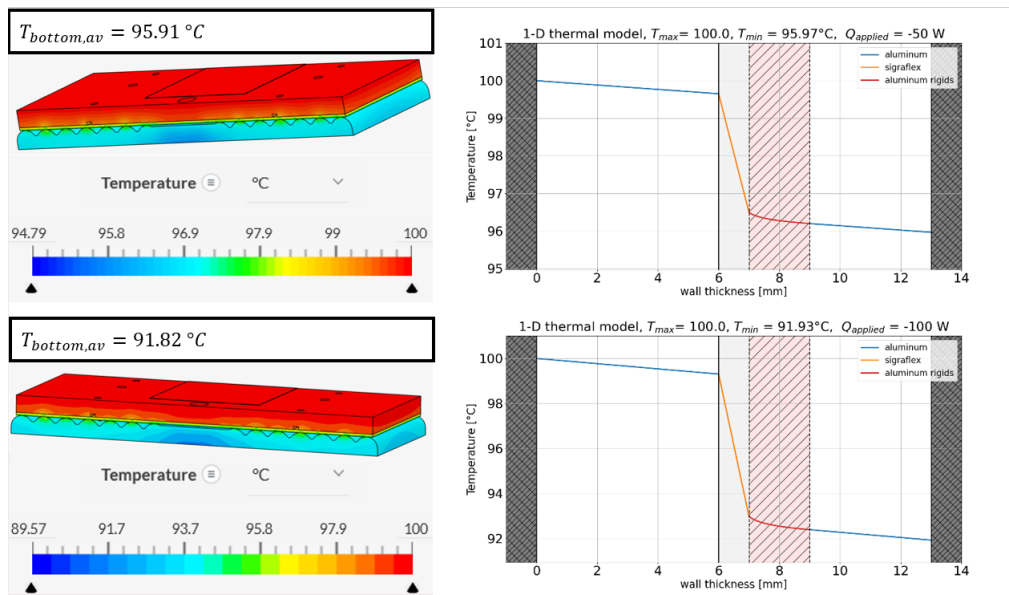


Figure 3.7: Comparison of simulations with the 1D constructed model for two different applied powers. Top left: Simulation for $Q_{applied} = 50W$, top right: model results for $Q_{applied} = 50W$, bottom left: Simulation for $Q_{applied} = 100W$, bottom right: model results for $Q_{applied} = 100W$. Material parameters used: $l_{sigraflex} = 0.8mm$, $k_{sigraflex} = 2.38W/mK$, $k_{aluminum} = 130W/mK$

More precisely, Table 3.2 shows the deviation of the model's temperature from the simulation. The deviation is calculated by dividing the difference in the temperature differences of the simulation and model, by the temperature difference of the simulation: $E = \frac{\Delta T_{simulation} - \Delta T_{model}}{\Delta T_{simulation}}$.

$Q_{applied}$	Percentage of deviation
50 W	1.5 %
100 W	1.3 %

Table 3.2: Deviation of the model's temperature difference across the mock-up surfaces from the simulations.

3.5 Cases studied

Multiple cases were investigated to understand the effect of various parameters on the conductivity and, eventually, optimize the interface parameters. The nominal parameters of the experiment concerning the flat mock-up are 2 sigraflex foils, 100% duty cycle and $5.2Nm$ applied torque. To present a holistic view of the conductivity and contact resistance behavior, the experiment was implemented for the same number of sigraflex foils and torque, with the duty cycle being varied to 80% and 60%. Since this property is not associated with the applied power, not a significant variation is expected. The next step is to keep the duty cycle constant at 100% while varying the applied torque in the range of $5.2Nm$ to $6.0Nm$, to check the effect the applied pressure on the mock-up has on the contact resistance. Lastly, both the duty cycle and the torque were kept constant at 100% and $5.2Nm$ respectively, while the number of sigraflex foils changed to 1, 3 and 4 as well as bare aluminum-aluminum. The overall case studies are summarized in Table 3.3.

Experiment cases				
Al-Al	1 foil	2 foil	3 foil	4 foil
100%, 5.2 Nm	100%, 5.2 Nm	100%, 5.2 Nm	100%, 5.2 Nm	100%, 5.2 Nm
-	-	80%, 5.2 Nm	-	-
-	-	60%, 5.2 Nm	-	-
-	-	100%, 5.6 Nm	-	-
-	-	100%, 6.0 Nm	-	-

Table 3.3: Description of the experiments performed. The percentage represents the duty cycle set in each session while the second number is the applied torque on the mock-up.

Since the modeling of the resistances is more complicated for the circular and negative case, using the values from the flat experiment the comparisons will be done in terms of temperature differences.

Chapter 4

Data post-processing

4.1 Clearing the data

The experimental procedure requires a constant power flux and not constant temperatures across the mock-up edges. The useful part of the data is where constant temperature difference is achieved across the mock-up edges. It is important to mention that all the calculations are done for every time instance of the measurements and then by using the useful part of the data, the values are averaged to take into account the uncertainty of the temperature measurements noise. A typical temperature graph is depicted in Figure 4.1.

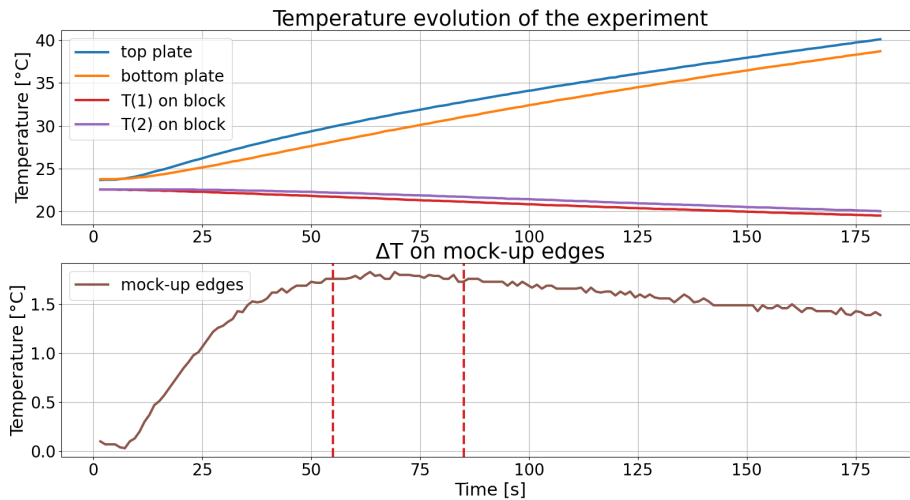


Figure 4.1: Typical experimental measurement graph. Top figure: temperature evolution on the different components used in the experiment. blue: temperature on the top of the mock-up, orange: temperature on the bottom of the mock-up, red: first temperature on the aluminum block, purple: second temperature on the aluminum block. Bottom figure: temperature difference on the mock-up edges with respect to time. The vertical red lines indicate the constant temperature difference part used for the analysis.

Initially, all the temperatures are almost equal to the ambient temperature. After the activation of the Peltier element, the sensor closer to it starts reading a temperature rise. In contrast, the sensor on the other side of the mock-up lags behind, due to the thermal resistance of the materials in between. A constant temperature difference is achieved approximately 50-60 seconds after the

beginning of the experiment and stays stable for approximately 30 seconds before decay starts. The decay of the temperature difference happens for two reasons. Convection losses increase with the increased temperature, and by increasing the temperature difference between the Peltier sides, its efficiency drops, delivering less power into the mock-up.

4.2 Identifying the applied power

Following from equation 2.10, the power on the mock-up is the sum of the absorbed power from the Peltier element and the electrical power applied to the Peltier. Since the mock-up is heated, power is absorbed from the aluminum block in contact with the cold side of the Peltier element.

The electrical power of the PWM signal is given by 4.1 [11] with V_{max} the maximum voltage of the pulse, I_{max} the maximum current of the pulse, and D the duty cycle of PWM. V_{max} and I_{max} are measured by a multimeter and correspond to the voltage and current applied from the motor driver to the Peltier element. However, since PWM is used, the measurements were done at 100% duty cycle, meaning DC. The voltage and current are calculated using equations 4.2 and 4.3, [11].

$$P_{eff} = V_{max} \cdot I_{max} \cdot D \quad (4.1)$$

$$V_{eff} = V_{max} \cdot \sqrt{D} \quad (4.2)$$

$$I_{eff} = I_{max} \cdot \sqrt{D} \quad (4.3)$$

It is observed that for all the experiments the voltage stays constant while the current drops as the Peltier element heat up. This will be taken into account in the uncertainty of the measurements.

For the power applied on the aluminum block, we will take advantage of equation 2.2. By tracing the time derivative of the block's temperature and knowing the aluminum type, hence its material properties, the power is estimated.

Since the experiment is conducted in air, the power calculated is not the power absorbed from the Peltier element, but rather the power absorbed along with the convection effect. So for an accurate calculation, the convective power needs to be calculated and subtracted.

The literature values for the convection coefficient in air vary between $5 - 25W/m^2K$ [12]. Calculating the convection power loss, with these numbers for the convection coefficient, will add a significant amount of uncertainty to the final result. To reduce the uncertainty, a different experiment is conducted to identify the convection coefficient of air in the lab.

The block of aluminum is heated with the assistance of the Peltier element and by using the Arduino's temperature controller, it reaches a constant temperature. To verify the uniformity of the temperature, two sensors 4 cm apart are used. When the desired temperature is uniformly achieved, the aluminum block was placed on top of a peek block, leaving 5 edges of the block exposed to air. The peek is used to minimize the heat transfer via conduction. The temperature evolution on the block is shown in Figure 4.2. The convection power is the one responsible for the temperature decrease of the block. By combining equations 2.2 and 2.8 and by numerically calculating the derivative of the temperature, the convection coefficient is determined from equation 4.4, derived by forcing equality on the two equations mentioned above.

The derivative is calculated by acquiring temperature and time data 100 samples apart, meaning if T_i is the n^{th} signal instance, T_f is the $n + 100^{th}$ instance. Δt is the time window equivalent to 100 time instances, which corresponds to $\approx 50s$. The time interval is appropriate as the cooling through convection is a slow process and the total experimental time is 20 minutes. The resulting convection coefficient $h_{convection}$ is shown in Figure 4.3

$$m \cdot c_p \frac{\Delta T}{\Delta t} = h_{conv} \cdot A_{exp} \cdot (T_{block} - T_{amb}) \Rightarrow h_{conv} = \frac{m \cdot c_p \cdot (T_f - T_i)}{A_{exp} \cdot (T_{block} - T_{amb}) \cdot \Delta t} \quad (4.4)$$

This way the uncertainty due to convection is greatly reduced since the span of the convection coefficient is minimized. The results are presented in Table 4.1. The convection coefficient is accurately measured and the power loss/gain due to convection can be subtracted from our calculations for any given temperature.

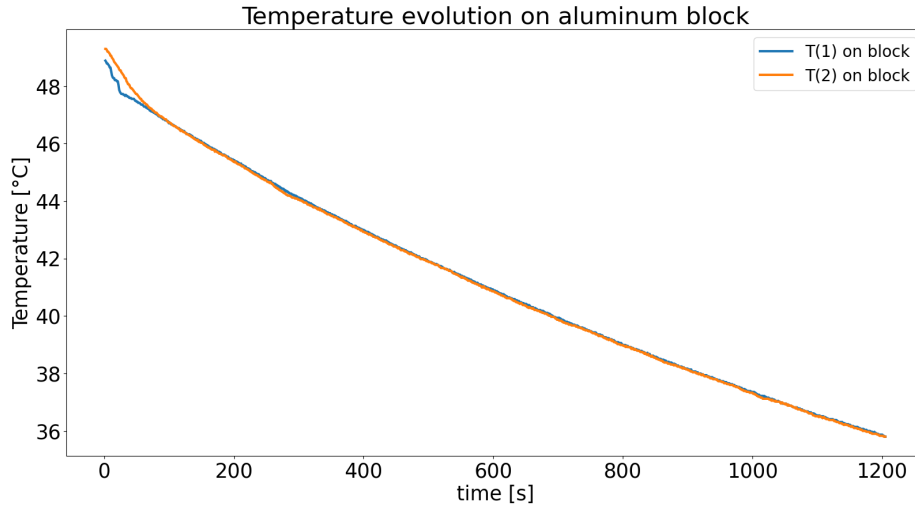


Figure 4.2: Temperature evolution on the aluminum block set on the top of the mock-up for the identification of the power absorbed from the Peltier element.

	$h_{literature} [W/m^2K]$	$h_{experimental} [W/m^2K]$
lowest	5	12.6
highest	25	12.7
deviation	20	0.1

Table 4.1: Convection coefficient comparison of literature and experimentally calculated values [3]

The measured power flowing out of the aluminum block contains the power absorbed from the Peltier element and the convective power. From the Peltier element power balance, the useful power component is the power absorbed from the Peltier element. To identify this component, the convective power is subtracted from the measured power.

The power delivered from the Peltier element to the mock-up is calculated by adding the electrical power to the latter identified component. However, the real power flowing through the mock-up, is the power delivered from the Peltier element minus the convective power on the mock-up.

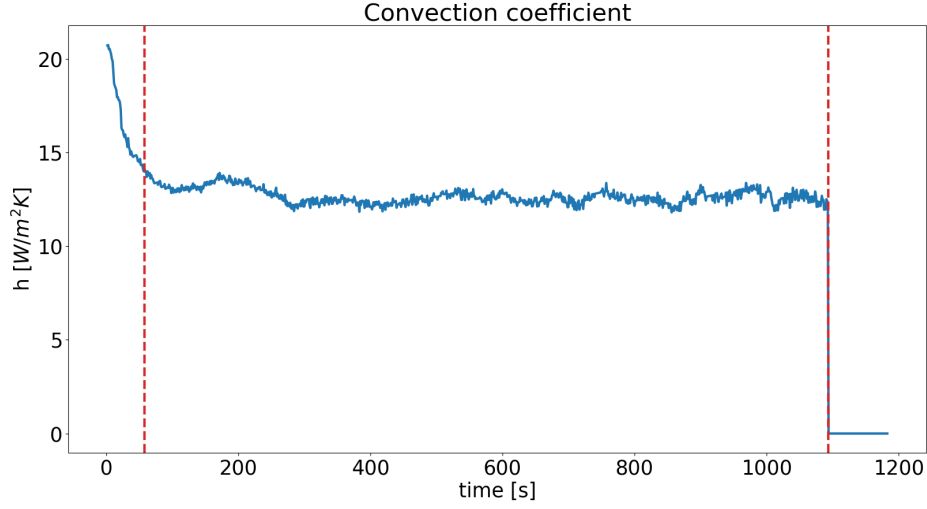


Figure 4.3: Calculated convection coefficient for the lab environment air. The red dashed lines indicate the valid part of the estimation

4.3 Effective conductivity

Initially, we will assume that there is perfect contact between the sigraflex and the aluminum parts. The term effective conductivity dictates that the inverse of the conductance is zero, meaning perfect material contact. When the applied power is known from the mentioned power analysis and the temperature difference is measured, using equation 2.3 the total thermal resistance of the mock-up is calculated. The total resistance includes both aluminum plates and the interface material (sigraflex). Equation 4.5 shows the sum of all the different thermal resistance parts.

$$R_{total} = R_{al,1} + R_{sigraflex} + R_{al,rigged} + R_{al,compact} \quad (4.5)$$

The thermal resistance of sigraflex is obtained by subtracting the total aluminum thermal resistance from the total resistance. Then, the conductivity of sigraflex is found by re-arranging equation 2.4 to equation 4.6.

$$R_{sigraflex} = \frac{l_{sigraflex}}{k_{eff} \cdot A_{plate}} \Rightarrow k_{eff} = \frac{l_{sigraflex}}{R_{sigraflex} \cdot A_{plate}} \quad (4.6)$$

4.4 Thermal contact conductance

For the previous assumption of perfect contact, the unknown variable is the conductivity of the interface material. Taking into account the imperfect contact, there are two unknown variables, namely, the conductance h_c and the conductivity of sigraflex $k_{sigraflex}$. Using the literature values for the conductivity of sigraflex, we will perform an estimation of the aluminum-sigraflex conductance, to investigate the effect of imperfect contact between the materials used in this experiment and gain an insight into the real case of steel-sigraflex.

The calculated thermal resistance of sigraflex contains three terms: the first aluminum-sigraflex contact resistance, the bulk resistance of sigraflex due to its conductivity and the second aluminum-sigraflex contact resistance with the reduced contact area. Those three terms are seen in equation 4.7 and the sigraflex conductance is calculated as seen in equation 4.8.

$$R_{sigraflex} = \frac{1}{h_c \cdot A_{plate}} + \frac{l_{sigraflex}}{k_{sigraflex} \cdot A_{plate}} + \frac{1}{h_c \cdot f \cdot A_{plate}} \quad (4.7)$$

$$h_c = \frac{1 + 1/f}{(R_{total} - R_{total,aluminum}) \cdot A_{plate}} \quad (4.8)$$

4.5 Data uncertainty

4.5.1 Materials

The main material used is aluminum AW5354 with properties well known. However, a 10% uncertainty is reasonable to exist in the conductivity and specific heat of the aluminum, as the manufacturing process of the material may cause imperfections in the internal structure of aluminum. For the sigraflex material, the uncertainty on its properties follows from the error propagation on the data analysis.

4.5.2 Measurements

Both power and temperature measurements have inherent uncertainty due to the deviation of their values. As mentioned in the previous sections, while the measured voltage was constant, variation was observed in the measured current and in the convection coefficient, eventually affecting the power applied to the mock-up.

Concerning the temperature measurements, uncertainty exists due to noise fluctuations and the assumption that the measured temperatures correspond to the mean temperature of the aluminum plates. For the first case, the uncertainty is easily calculated by viewing the signal at the chosen part and by calculating the mean and standard deviation of the measurement. The second case needs investigation to confirm that the claim is valid, otherwise, extra uncertainty is present, due to the difference between the mean temperature and the temperature at the measurement point.

Since the average temperature of each plate is not known in this setup, simulations will be performed in SimScale to validate, for the parameters used and values found in the experiment, to what extent the temperature in the measurement point matches the mean temperature of the plate.

The simulation program does not take into account conductance, meaning that in the contact areas, perfect contact is assumed. In order to import the correct conductivity for the interface material, the effective conductivity is used, to include the effect of imperfect contact. Because of the existing material uncertainty, the calculated conductivity also varies. Hence, for each case study, two simulations are performed, with the highest and lowest value of the effective conductivity calculated. Since the experiment is performed with varying temperatures but with constant temperature differences between two points, we check for agreement between the two results, i.e. if the temperature difference measured experimentally matches the simulation predictions within their error range. If it does, this means that the simulation is accurately representing the experiment.

For the last step, we check if the temperature at each sensor position matches, or is close, to the average temperature of the respective aluminum plate. If the value is lower than the error induced by the sensors, then we can safely assume that the temperature in the sensor position is equal to the mean temperature of the plate. If the temperature between the sensor position and the mean value varies significantly, an extra uncertainty will be induced in the experimental temperature data. A new effective conductivity needs to be calculated and the same validation procedure must be repeated.

Chapter 5

Results

5.1 Conductivity estimate.

After calculating the power applied on the mock-up and the thermal resistances using the analysis mentioned in chapter 4, the effective conductivity is estimated. Figure 5.1 depicts a typical estimation of the conductivity of the thermal interface material. As stated the calculations were made for each time instance of the chosen time window and are averaged to include the uncertainty of the temperature measurements. A comparison with the rest of the experimental case studies will follow. As a reminder, Table 4.1 summarizes all the experimental parameters for all the case studies.

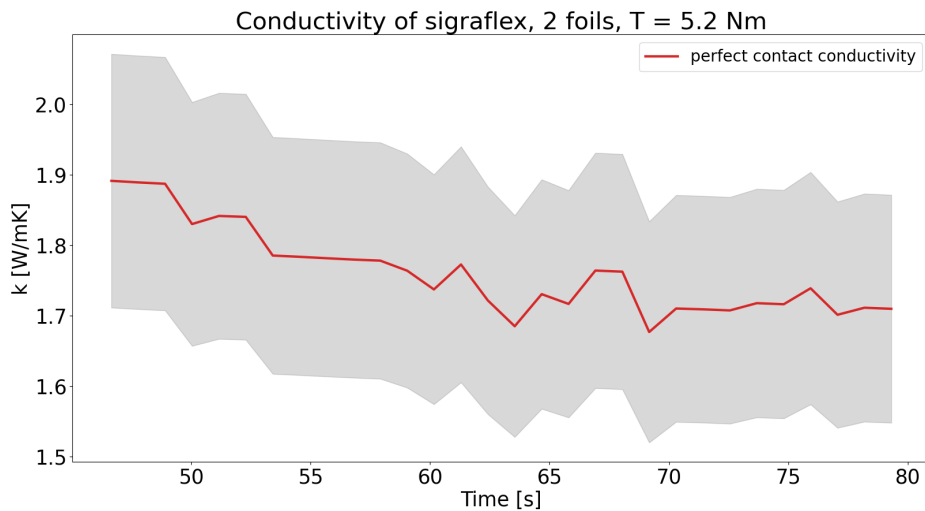


Figure 5.1: Estimated thermal conductivity of sigraflex, for the assumption of perfect thermal contact with aluminum. The grey area represents the uncertainty of the calculation.

One supplementary way to validate experimentally that the calculations done in the code are correct is by checking the conductivity of sigraflex for different applied powers. Since conductivity is not a property dependent on power it should remain constant. Indeed as it is seen in Figure 5.2, a small deviation between the mean values exists with an overlap in the conductivities, including the uncertainties. In any case, we can assume that the experiment and the data processing are accurate.

The first case study depicted in Figure 5.3, is the variation of the applied torque while keeping

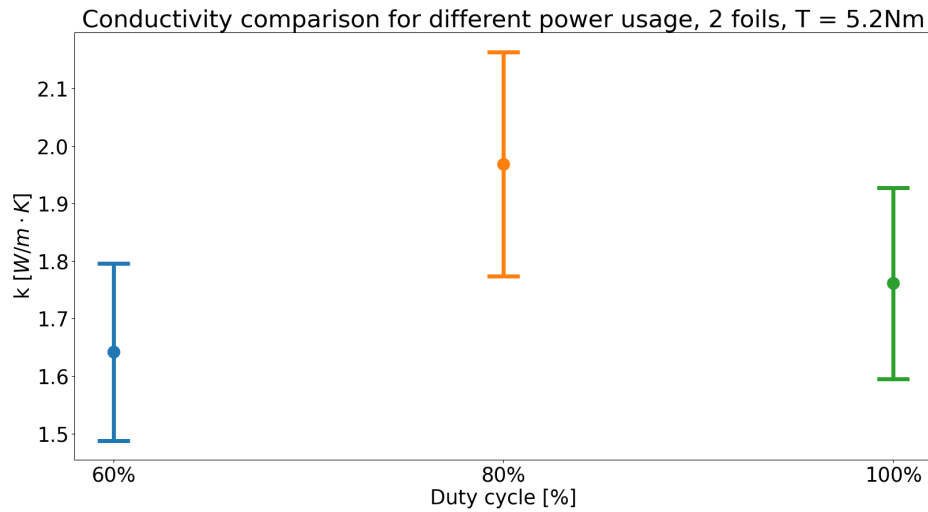


Figure 5.2: Thermal conductivity of sigraflex comparison, for the assumption of perfect thermal contact with aluminum, for the case study of different applied powers.

the power constant at 100% duty cycle, using 2 sigraflex foils. The intuitive outcome is to observe an increase in the conductivity with the increase of the applied torque, as the contact becomes better and the flexibility of sigraflex covers more area at the ridged side.

The result deviates from the expected as, for the 5.6 Nm case, a relative decrease exists before the 6.0 Nm relative increase. This behavior has two possible explanations. While the torque was applied, bending of the aluminum was observed, potentially reducing the contact area between aluminum and sigraflex more than anticipated, causing a decrease in the calculated conductivity. With even higher torque the effect was still visible, but as an addition, the middle flat part of the mock-up was in contact with sigraflex, causing an increase in the calculated conductivity. The second explanation involves the chosen torque values. The 6.0 Nm torque was already enough for the mock-up to bend visibly and the 5.2 Nm torque was the lowest possible that it could be applied. Hence, the torque effect was subtle and not observable.

The next case study considers the effect of multiple sigraflex foils. Figure 5.4 shows the behavior of the effective conductivity for a different number of sigraflex foils, while the power is kept at 100% duty cycle and the torque at 5.2 Nm. For this case, a clear difference between the use of different sigraflex foils appears, with the worst case appearing for 1 sigraflex foil and a significant increase for the 2-foil and 3-foil conductivities, while for the 4-foil case, saturation starts. The difference between the nominal case of 2 foils with the 1 foil and 3-4 foils cases can be attributed to the worsening and improvement respectively of the contact both between the sigraflex and the mock-up, but also between the sigraflex foils themselves. As sigraflex foils increase their thickness, they also become more compact, without losing their flexibility. Hence the contact area increases up to the point where conductivity saturates.

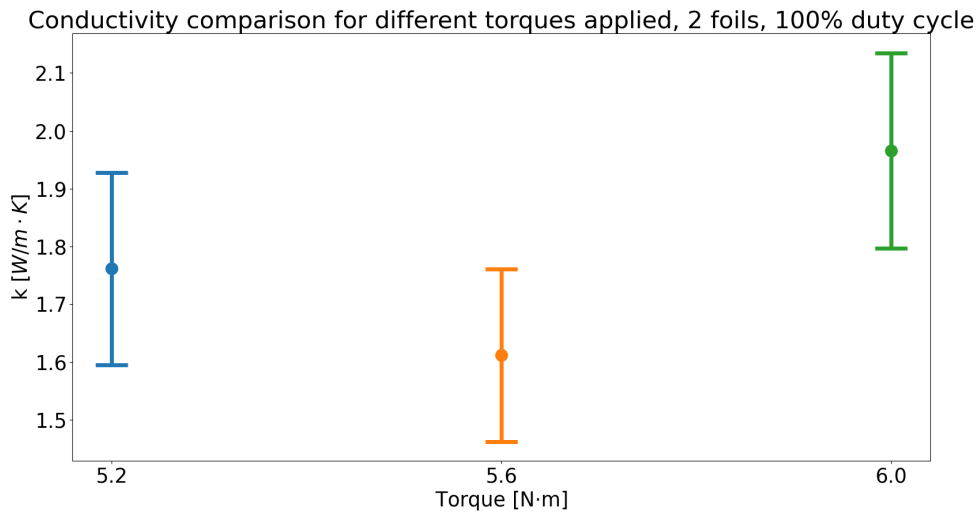


Figure 5.3: Thermal conductivity of sigraflex comparison, for the assumption of perfect thermal contact with aluminum, for the case study of different applied torques.

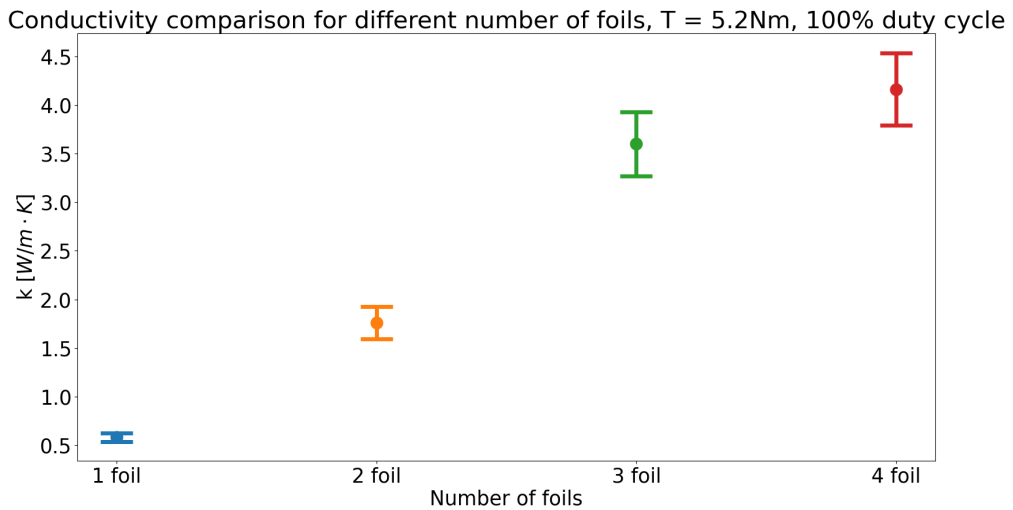


Figure 5.4: Thermal conductivity of sigraflex comparison, for the assumption of perfect thermal contact with aluminum, for the case study of different numbers of foils.

5.2 Thermal contact conductance estimate.

For the assumption of imperfect contact, literature values for the conductivity of sigraflex are used to calculate the conductance of aluminum-sigraflex for all the case studies.

The thermal resistance of sigraflex estimated from the experimental results contains 3 terms: the conductance of the first contact of the mock-up, the bulk thermal resistance of sigraflex which is a product of the sigraflex's conductivity and the conductance of the second contact with the reduced contact area. Normally the dominant factor in the thermal resistance of an interface is the bulk resistance of the interface. In this case, one contact has a reduced area and hence an inspection of the individual terms must be done to get an insight into which part is dominant. For the calculation of the thermal resistances, it is assumed that the conductivity of sigraflex is the one mentioned in the literature [13] for the sigraflex thickness matching the one used in the experiment, equal to $k = 5.95W/mK$.

Figure 5.5, shows the contribution of each term in the total thermal resistance. Comparing the top with the middle plot it is visible that the bulk thermal resistance is approximately 4 times larger than the first contact resistance. When the area is reduced, however, the resistance increases and, as shown in the bottom plot, the dominant part is the contact on the reduced area.

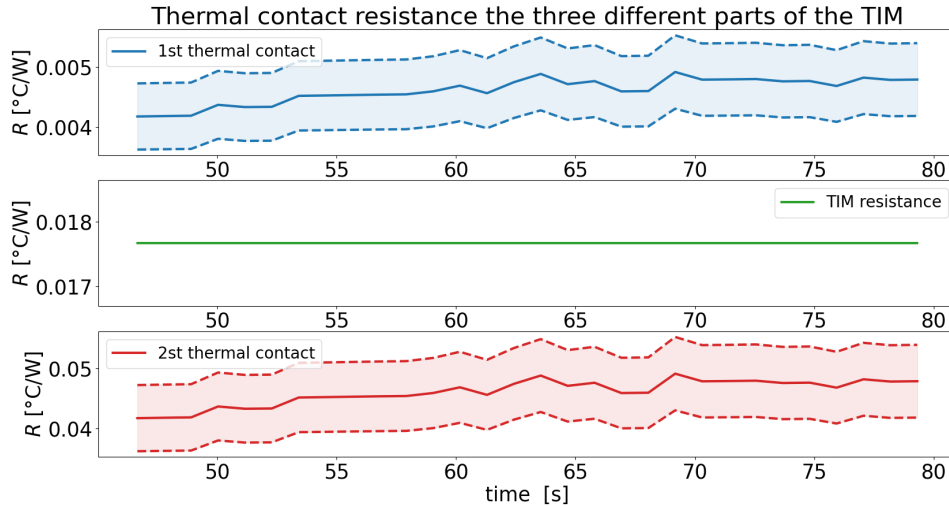


Figure 5.5: Break-up of the individual parts of the interface thermal resistance. Top: first contact part, middle: sigraflex bulk part (The term "TIM" refers to "Thermal Interface Material"), bottom: second reduced area part.

For the conductance of the interface aluminum-sigraflex, as seen from equation 2.9, its behavior for the first two case studies is the same as the conductivity. For completeness purposes, Figure A.1 shows the statement above in the Appendix A, and hence no further explanation is needed for those graphs.

The bare aluminum-aluminum contact was tested under the same experimental parameters, meaning applied torque of $5.2 Nm$ and duty cycle of 100 %. Figure 5.6 shows the comparison of the conductance of aluminum-sigraflex for the different case studies with the aluminum-aluminum conductance.

The conclusion drawn from this graph is that the sigraflex interface significantly improves the thermal contact of the mock-up, and bare metal contact is not efficient enough for implementation in the real bolometer camera, as the contact will worsen the heat transfer.

Moreover, to verify this claim, Figure 5.7 compares the thermal resistance of aluminum-aluminum interface with the worst case which is the 1 sigraflex foil. It becomes obvious that

even with 1 sigraflex foil, the thermal resistance is almost 3 times smaller, meaning the temperature difference from one side of the interface to the other will be 3 times larger for the aluminum-aluminum case.

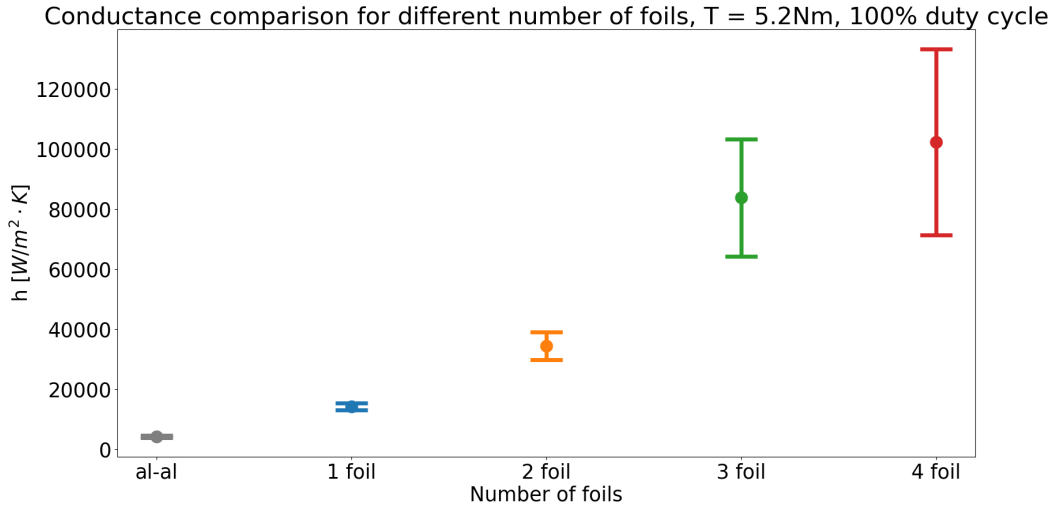


Figure 5.6: Comparison of thermal contact conductances for the different number of foils along with the aluminum-aluminum case.

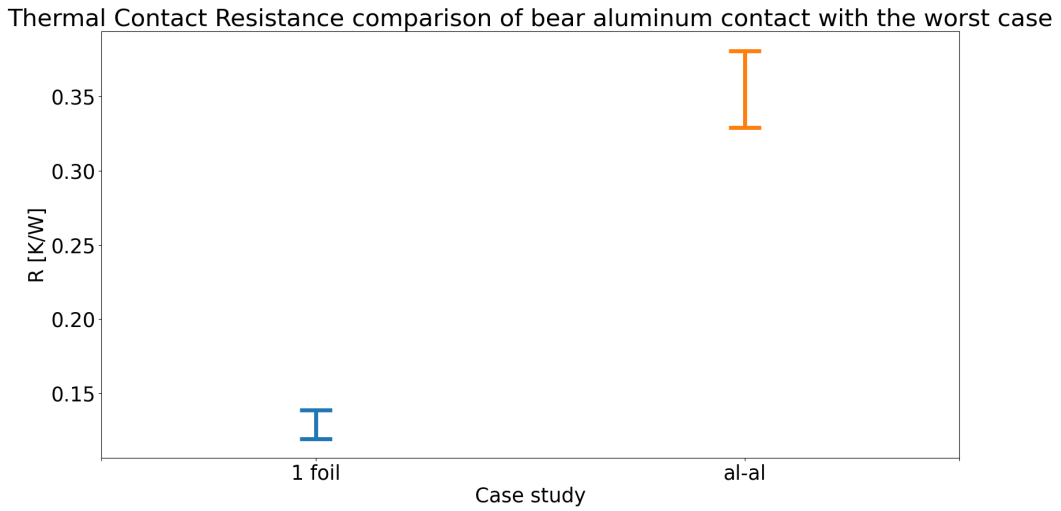


Figure 5.7: Comparison of thermal contact resistances for the different interface materials.

5.3 Validation of the results.

The processing mentioned in this chapter assumed that the sensor temperatures at the mock-up sides are equal to the mean temperature of the mock-up plates. To validate this claim, using the conductivity numbers found from the experiment for the respective applied powers, simulations are performed to show the deviation of the temperature in the sensor positions from the mean temperature of the plates. Since the conductivity of the interface has uncertainty, for each experiment and plate, 2 simulations are done for the lowest and highest conductivity value found.

As seen in both Figure A.2 and Figure A.3, the deviation of the sensor position temperature from the mean is small compared to the total temperature gradient along the plates. Hence it is safe to assume that no extra uncertainty needs to be introduced and that the results are accurate.

Furthermore, Figure 5.8 shows the deviation of the experimental temperature difference from the simulated, for the calculated conductivity values. For the majority of the experiments, there is agreement between the simulated and experimental temperature differences, with the exception of the first case representing the 1 sigraflex foil. Indeed this case was problematic, due to the low stiffness of sigraflex causing miscalculation of the contact area. The experimental results produce a higher temperature difference value compared to the simulation for the same conductivity, meaning that the conductivity, or better the contact area, is overestimated.

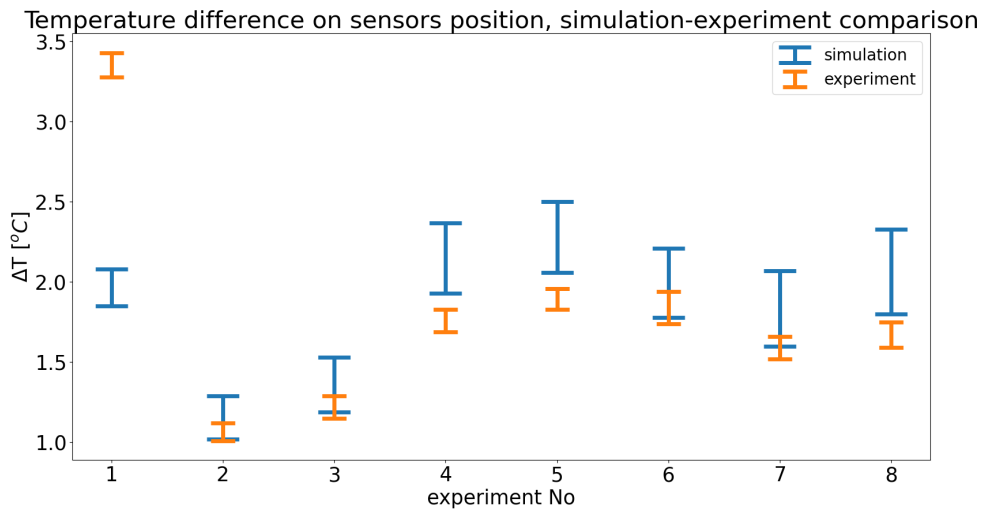


Figure 5.8: Comparison of the simulated temperature difference across the flat mock-up (blue) with the experimental temperature difference (orange).

5.4 Curved and negative mock-ups

The 1D model is valid only for the flat mock-up. A few attempts to modify the model to fit the curved mock-up resulted in mismatches with simulations. Hence the modeled thermal resistances are not representing the real setup accurately. The only analysis that can be performed, is a comparison of the experimental temperatures acquired with the simulation model. In this comparison, the perfect contact conductivity found for the flat part will be used in the simulations, as the interface material and contact material do not change and this property should also remain unchanged.

The comparison is done by taking the simulation data of the sensor positions and by using the same applied power as in the experiment. In Figure 5.9 the simulation shows a higher ΔT than the experimental case, meaning that the conductivity calculated is underestimated.

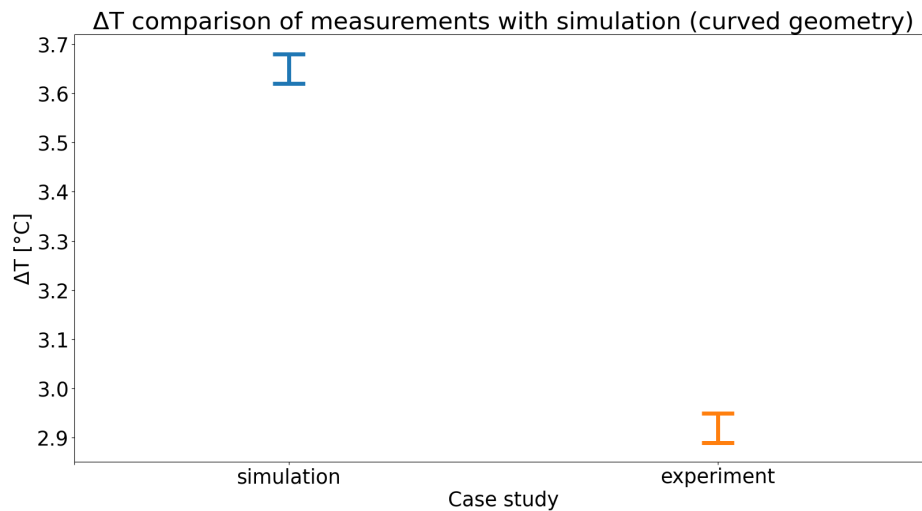


Figure 5.9: Comparison of simulation and experimental data for the achieved ΔT for the curved mock-up.

This result is well justified by the higher stiffness of the more compact aluminum mock-up. As mentioned, the flat mock-up showed signs of bending while applying the torques, reducing the actual contact area of the plates with the sigraflex. With the curved part having a higher stiffness, the contact area increases significantly, as the bending, in this case, is trivial. It is worth mentioning that steel, which will be used in the real CBC, has also a higher stiffness compared to aluminum. This means that the same behavior is expected for the real case, i.e. the conductivity found is underestimated.

For the negative base of the CBC, the experiment did not produce a long enough time window where the temperature difference was constant. For this reason, we present the temperature difference between the mock-up sides compared with the temperature difference of the flat mock-up for the same parameters in Figure 5.10. This graph proves that the effect of the contact area is crucial for an effective heat transfer.

The negative mock-up, matches almost perfectly the portliner pipes geometry, increasing dramatically the contact area of sigraflex with the portliner. This is translated in lower temperature difference values by a factor of more than 2 compared with the flat mock-up for the same experimental parameters (Table 5.1)

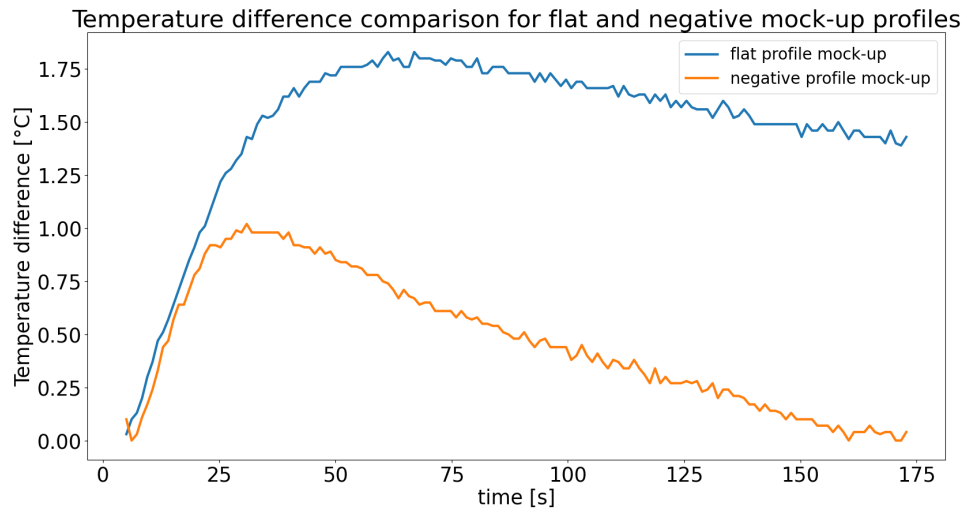


Figure 5.10: Comparison of the temperature difference between the flat and negative CBC base mock-up.

Duty cycle [%]	Torque [Nm]	Foil No
100	5.2	2

Table 5.1: Experimental parameters for the negative CBC base mock-up.

5.5 Steel-sigraflex extrapolation analysis

So far we have identified the conductivity of the sigraflex foils assuming perfect contact and the conductance of sigraflex-aluminum by using the literature conductivity value of sigraflex. The conductance values are not transferable between materials, although [3] mentions the conductance of graphite with metals to be in the same span. To the author's knowledge, no literature values for steel-graphite foils were found.

Assuming perfect contact, we will use the 1D model inputting steel material properties and the sigraflex thermal resistance found, to investigate the expected temperature difference between the base of the CBC and the portliner, for reactor-relevant heat loads. From data taken from the Max Planck Institute of Plasma Physics, for the ports where the CBC is planned to be mounted, the maximum expected heat load is $120kW/m^2$.

From Figure 5.11 the lowest temperature difference occurs for case study No 7. As a next step, we will perform an investigation of the effect of the conductance for this case. Since no data concerning the steel-sigraflex conductance exist, we will manually vary the conductance of steel-sigraflex, assuming that the conductance of this interface is equal or lower than the one of aluminum-sigraflex.

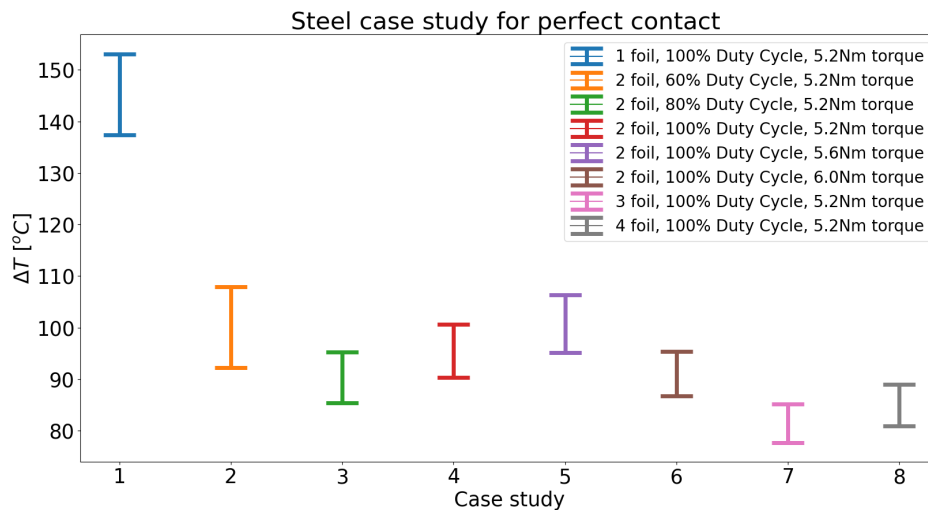


Figure 5.11: Temperature difference across the mock-up for steel properties. The results were produced from the 1D model, for steel conductivity: $k_{steel} = 45 W/mK$ and for the sigraflex parameters of each experiment. The applied power flux: $120 kW/m^2$

From Figure 5.12, it seems that for most of the conductance cases, the temperature difference remains relatively low. The effect of the conductance becomes dominant only for low values. It is worth mentioning that the last case is close to the conductance of bare steel-steel and since it was observed that sigraflex increases the thermal heat transfer for the aluminum case, it is safe to assume that the same will happen for the steel case.

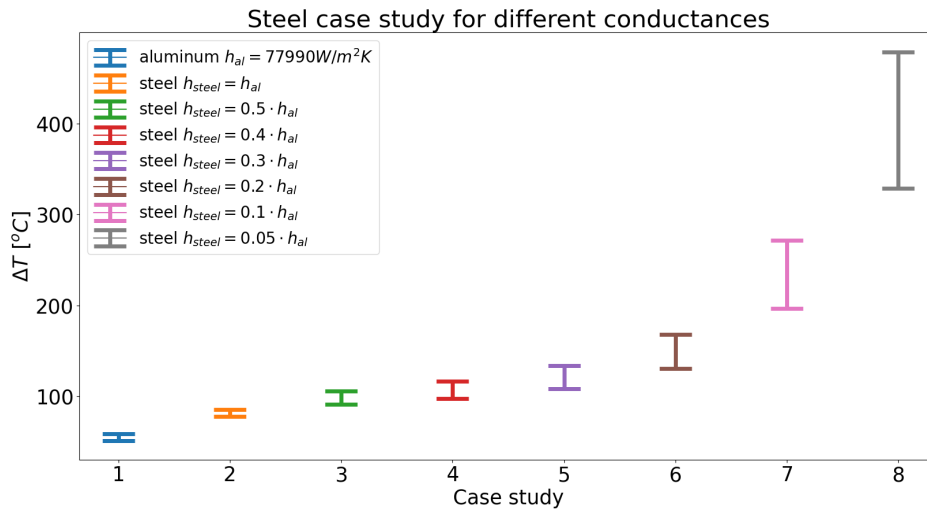


Figure 5.12: Investigation of the conductance variation of the steel-sigraflex contact on the heat transfer, for the reactor-relevant heat load of 120 kW/m^2 . The reference of this analysis is the best case of the aluminum case study (marked in blue) taken from Figure 5.11. The investigated conductance values are random due to the lack of evidence for the thermal contact conductance of steel with sigraflex.

5.6 Simulations on the full CBC model

For the final part of the report, we perform a simulation in SimScale using the calculated conductivity from the experiments to confirm that the parts of interest can withstand the heat load of the reactor. The simulation is done for the conductivity value $k = 2.5 \text{ W/mK}$, which is an underestimation of the best case scenario as a safety factor. As boundary conditions, a heat load of 120 KW/m^2 is applied, corresponding to the highest heat load the camera is expected to receive in the ports and a constant temperature of $30 \text{ }^\circ\text{C}$ in the portliner surface is set, corresponding to the temperature of the flowing fluid inside the portliner pipes.

For this simulation, due to software limitations, certain simplifications are made. The heat load is set on the front face of the CBC and the constant temperature is set on the contact surface of the CBC base with the portliner pipes. In reality, the heat load is applied to the full cross-section of the portliner (the heat load on the CBC face is overestimated for the simulation) and the constant temperature is the temperature of the fluid, ignoring the heat transfer through convection between the fluid and the steel pipes.

Figure 5.13 shows the result of the simulation for the boundary conditions mentioned, after 5 minutes of heat load, which corresponds to the longest experimental time. The normal experiment length timewise in W7-X is 10 seconds of loading and 15 minutes of cooling down. The simulation shows that the maximum temperature reached for the steel parts is $411.6 \text{ }^\circ\text{C}$. For the base plate of the bolometer channels, the mean temperature of the plate is increased by $0.04 \text{ }^\circ\text{C}$. This result is crucial, because it proves that for the worst case scenario in the reactor, the camera can withstand the heat load, while the channel plate remains at the same temperature. If the channel plate was heated, the channels would produce inaccurate bolometer measurements due to temperature drifts and complicated calibration would be necessary for the CBC to work properly.

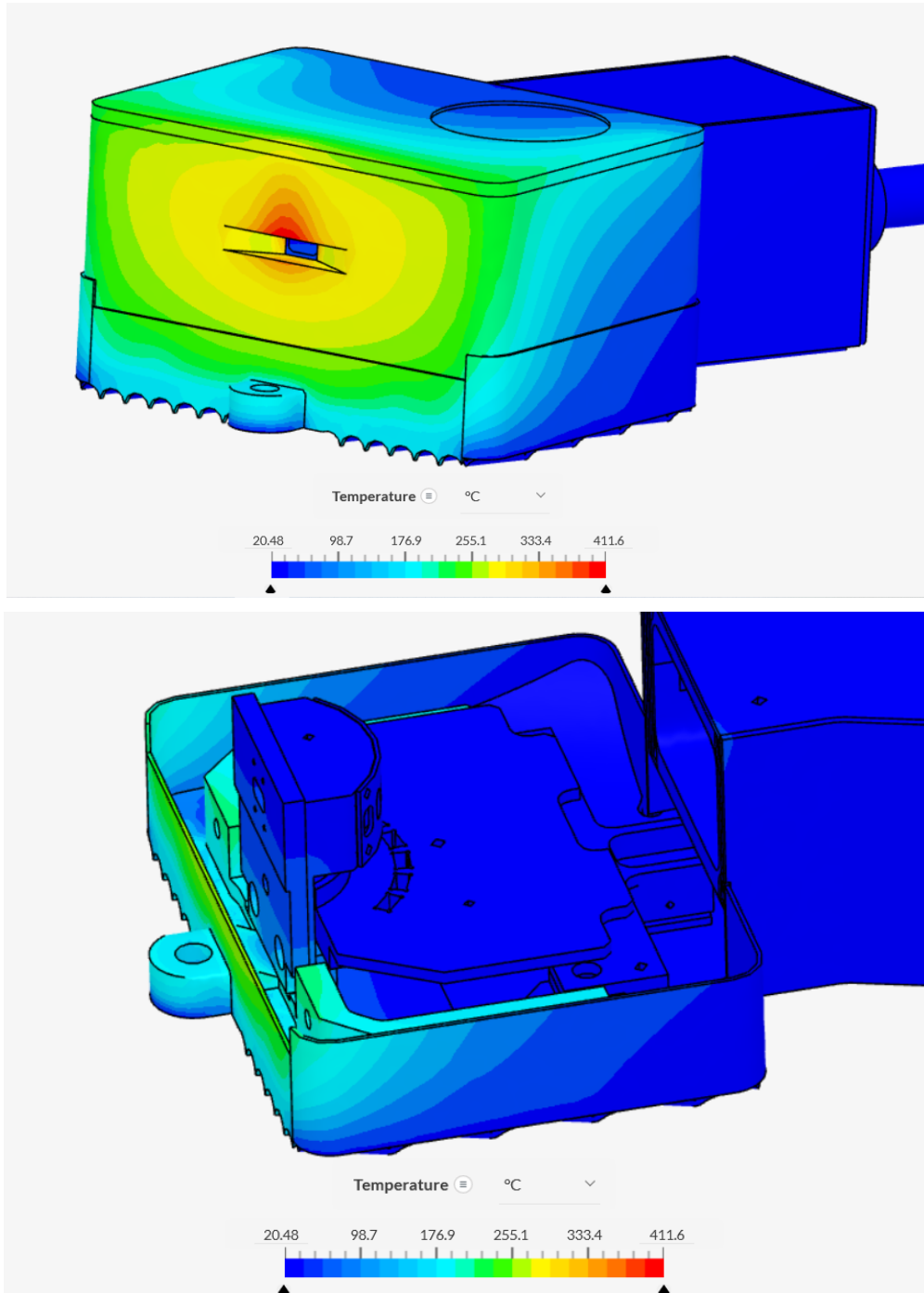


Figure 5.13: Simulation on the full CBC model. Top: outer view of the CBC model, Bottom: inside view of the CBC model. The channel base plate is indicated with the arrow

Chapter 6

Conclusions

Despite the experiment alternation, the analysis in this report provides validation of the interface material conductivity for the heat transfer between the base of the CBC and portliner of the W7-X reactor. It is the author's opinion that the alternate experiment complicated the procedure more than the case with the constant temperatures. Extra steps were needed to provide accurate results that would be unnecessary if the experiment was implemented in vacuum with constant temperatures across the mock-up edges.

From the results, we can conclude that sigraflex foil as an interface material, improves heat transfer compared to bare metal-metal contact, as it increases the contact area between the two parts, and that the interface conductivity values used in the simulations of the CBC for the approval of the design, were of the same order of magnitude. In vacuum conditions, where the only heat transfer mechanisms are conduction and radiation, the contact area of the materials plays a crucial role. The case study with the negative part of the portliner in the CBC base proves this point. The negative part of the portliner was the most effective geometry tested in terms of heat transfer, with the lowest temperature difference across its edges.

The effect of the applied torque seems to be insignificant for the heat transfer. However, the increase in the number of foils shows improvement in the heat transfer performance, up until saturation. Furthermore, the mounting position (flat or circular part of the portliner) is trivial, as it is shown that for both the flat and curved mock-ups the heat transfer is sufficient.

The optimal setup for the camera installation is with 3 sigraflex foils and a negative-of-the-pipes profile for the base of the CBC. The manufacturing process of the base cannot produce an exact negative profile of the pipes, as the portliners have slightly different profiles depending on the mounting position, but in any case, compared to the flat case for the base, the contact area will be improved.

The results were cross-checked with simulations with the same parameters as in the experiments. Moreover, using the experimental results of the interface material for the full CBC model simulation, the results prove that the camera can withstand the worst-case scenario heat flows for 5 minutes, which is the maximum experimental time of the reactor for the current experimental campaign. Unfortunately, due to software limitations, the cyclic heating scenario was not investigated. It is suggested before the installation to perform this analysis to verify that the time between discharges is enough for the camera to cool off.

For performing similar experiments in the future, the author recommends the following:

- Peltier elements are of low-performance for creating constant temperatures. Instead thermal elements can be used (resistors) for heating one side because their power can be easily calculated by current and voltage measurements, along with active cooling to allow the heat a medium to be dissipated.
- Vacuum remains the ideal environment for these experiments both because of the increase in the accuracy of the results and due to the imitation of the reactor's conditions.

Bibliography

- [1] Zhang D. et al. Bolometer tomography on Wendelstein 7-X for study of radiation asymmetry. *Nuclear Fusion*, 61:116043, 2021. doi: 10.1088/1741-4326/ac2778. 1
- [2] Bosch H.-S. et al. Construction of Wendelstein 7-X - Engineering a steady state stellarator. *23rd IEEE/NPSS Symposium on Fusion Engineering, San Diego, CA, USA*, pages 1–7, 2009. doi: 10.1109/FUSION.2009.5226367. 1
- [3] Lienhard J.H. IV and Lienhard J.H. V. *A Heat Transfer Textbook, 5th ed.* 2000. 5, 19, 31
- [4] Ruifeng D., Tianran G., Xunliang L., and Zhi W. Effects of contact pressure, interface temperature, and surface roughness on thermal contact conductance between stainless steel surfaces under atmosphere condition. *International Journal of Heat and Mass Transfer*, 94: 156–163, 2016. doi: <https://doi.org/10.1016/j.ijheatmasstransfer.2015.11.069>. 6
- [5] Riffat S.B. and Ma X. Improving the coefficient of performance of thermoelectric cooling systems: a review. *Energy Research*, 10:753–768, 2004. doi: <https://doi.org/10.1002/er.991>. 6, 7
- [6] Kumar S. and Mahto D. Thermal Analysis and Performance Evaluation of Peltier Module. *Renewable Energy and its Innovative Technologies*, 93:173–184, 2019. doi: https://doi.org/10.1007/978-981-13-2116-0_14. 7
- [7] Solfiti E. and Berto F. A review on thermophysical properties of flexible graphite. *Procedia Structural Integrity*, 26:187–198, 2020. doi: <https://doi.org/10.1002/er.991>. 11
- [8] Elsey R.J. Outgassing of vacuum materials-I: A paper in our educational series: The theory and practice of vacuum science and technology in schools and colleges. *Vacuum*, 25:299–306, 1975. 11
- [9] Xiaogang Li, Renxi Luo, Weifang Zhang, and Haitao Liao. Method for measuring thermal contact resistance of graphite thin film materials. *measurement*, 93:202–207, 2016. doi: <https://doi.org/10.1016/j.measurement.2016.07.015>. 12
- [10] SimScale platform. <https://www.simscale.com/product/>. 14
- [11] Rawlings J.C. *Basic AC Circuits, 2nd Edition.* 1981. 18
- [12] Kosky P., Balmer R., Keat W., and Wise G. *Exploring Engineering: An Introduction to Engineering and Design 5th edition.* 2020. ISBN <https://doi.org/10.1016/C2017-0-01871-2>. 18
- [13] Sabau A.S. Review of thermal contact resistance of flexible graphite materials for thermal interfaces in high heat flux applications. 2022. doi: <https://doi.org/10.2172/1896991>. 26

Appendix A

Appendix

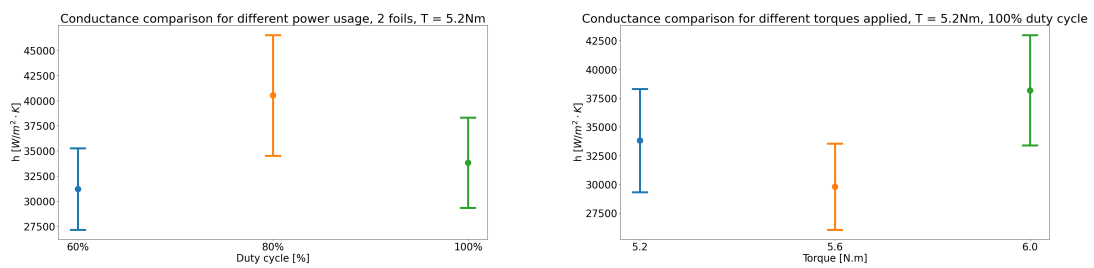


Figure A.1: Calculated conductances for the two case studies. Right: different applied power, left different applied torque.

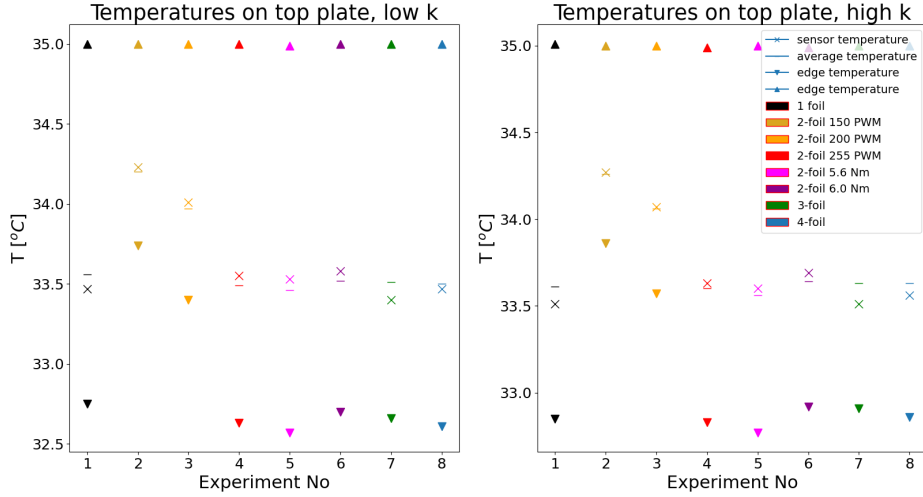


Figure A.2: Simulated temperatures on the top mock-up plate. Temperatures were taken in the middle of the plate, sensor position, edge of the plate and average temperature of the plate. Left: simulation for the low found conductivity, right: simulation for the high found conductivity.

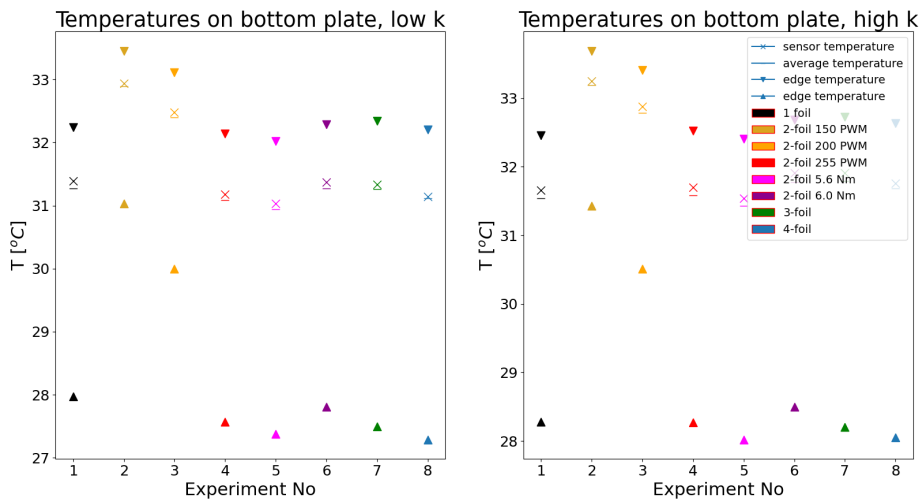


Figure A.3: Simulated temperatures on the bottom mock-up plate. Temperatures were taken in the middle of the plate, sensor position, edge of the plate and average temperature of the plate. Left: simulation for the low found conductivity, right: simulation for the high found conductivity.